RSC Advances

PAPER

View Article Online
View Journal | View Issue

Open Access Article. Published on 01 September 2017. Downloaded on 11/23/2025 1:03:58 PM.
This article is licensed under a Creative Commons Attribution 3.0 Unported Licence.

Check for updates

Cite this: *RSC Adv.*, 2017, **7**, 42350

Investigation on the properties of Ta doped Ti_3SiC_2 as solid oxide fuel cell interconnects

Lili Zheng,[*ab] Qingsong Hua,[a] Xichao Li,[*bc] Meishuan Li,[b] Yuhai Qian,[b] Jingjun Xu,[b] Zuoqiang Dai,[a] Tao Chen,[a] Jianmin Zhang[a] and Hongxin Zhang[a]

Received 29th June 2017
Accepted 14th August 2017

DOI: 10.1039/c7ra07215e

rsc.li/rsc-advances

The oxidation behaviours and electrical properties of 5 at% Ta doped Ti_3SiC_2 solid solution have been investigated at 800 °C in air for up to 500 h. The oxidation kinetics of $(Ti_{0.95}Ta_{0.05})_3SiC_2$ follows a parabolic law. The oxidation rate constant is 7.33×10^{-14} g^2 cm^{-4} s^{-1}, which is lower than those of Ti_3SiC_2, $(Ti_{0.95}Nb_{0.05})_3SiC_2$ and Crofer 22 APU. Ta doped r-TiO_2 formed $(Ti_{0.95}Ta_{0.05})_3SiC_2$ during the oxidation process. Ta doping can limit the outward diffusion of Ti by decreasing the native Ti interstitials concentration and simultaneously restraining the inward diffusion of oxygen by decreasing the O vacancy concentration. As a result, the oxidation resistance is significantly improved and the oxide scale structure of Ti_3SiC_2 changes from a double-layer to a monolithic layer. The ASR of $(Ti_{0.95}Ta_{0.05})_3SiC_2$ after oxidation at 800 °C in air for 500 h is 29.5 mΩ cm^2, which is much lower than that of Ti_3SiC_2. Ta doping can increase the electron concentration in r-TiO_2 and thereby increase the electrical conductivity of r-TiO_2. Therefore, the ASR of $(Ti_{0.95}Ta_{0.05})_3SiC_2$ after oxidation is lower compared to that of Ti_3SiC_2.

1. Introduction

Due to concerns relating to the energy crisis and environmental deterioration, solid oxide fuel cells (SOFC), as one of the promising clean energy technologies, have drawn much attention. SOFC possesses many advantages, such as high efficiency, fuel flexibility, and low contribution towards pollution. It is an electrochemical device which generates electricity and heat from fuel and produces chemical energy without combustion.[1,2] For SOFC commercialization, interconnects are an essential part. Interconnects are used to build up multiple cell-stacks from the single cell. It plays two roles: (1) acts as the physical separator of fuels in the anode cavity and air or oxygen in the cathode cavity; (2) acts as the bipolar plate electrically connecting adjacent cells in series.[3] The requirements for interconnect materials are strict and include the following: good electrical conductivity; good oxidation, corrosion, and carburization resistance; adequate stability in terms of dimension, microstructure, chemistry and phase at operating temperature in oxidizing and reduction environments; gas tightness; appropriate thermal expansion coefficient, and no reaction and inter-diffusion with adjacent components.[2–4] Over the past decades, $LaCrO_3$ and doped $LaCrO_3$ have been widely studied as interconnects for SOFC. However, there are many native defects, which hinder its extensive development, such as difficulty in sintering and machining of compact chromite parts and high manufacturing costs.[2] As the working temperature of SOFC decreases to intermediate temperature (600–800 °C),[5–7] metal becomes the main material used as the interconnect. Metallic interconnects have many advantages, such as high electrical and thermal conductivity, low cost, easy manufacture and good workability.[8,9] However, all metallic interconnects have the "chromium oxide poison" problem. The main oxide formed on the metallic interconnect is Cr_2O_3. Cr species evaporation can poison the cathode and the cathode/electrolyte interface and result in the degradation of performance of SOFC.[10] Also, the stepwise increase in area specific resistance (ASR) of surface scale hinders the development of metallic interconnects. To overcome these problems, various new kinds of alloys[11–20] and coatings[21–28] have been explored. However, these issues have not been completely resolved. Therefore, more efforts are needed to develop a novel Cr-free interconnect material. It should possess good oxidation resistance as well as post-oxidation superficial electrical conductivity.

MAX phases are a group of layered ternary compounds, marked as $M_{n+1}AX_n$ (M: early transition metal, A: IIIA or IVA element, X: C and/or N). They have attracted significant attention due to the merits of both ceramics and metals. Ti_3SiC_2, one of the most typical MAXs, possesses unique properties, such as low density, high modulus and fracture toughness, high electrical and thermal conductivity, easy machinability, good resistance to oxidation and thermal shock below 1100 °C.[29,30] However, the oxidation resistance of pure Ti_3SiC_2 at a working temperature cannot satisfy the requirements of interconnects.

[a]Power & Energy Storage System Research Center, College of Mechanical & Electronic Engineering, Qingdao University, Qingdao, 266071, China
[b]Shenyang National Laboratory for Materials Science, Institute of Metal Research, Chinese Academy of Sciences, Shenyang 110016, China
[c]Qingdao Institute of Bioenergy and Bioprocess Technology, Chinese Academy of Sciences, Qingdao, 266101, China. E-mail: lixc@qibebt.ac.cn

 This journal is © The Royal Society of Chemistry 2017

Open Access Article. Published on 01 September 2017. Downloaded on 11/23/2025 1:03:58 PM. This article is licensed under a Creative Commons Attribution 3.0 Unported Licence.

One of the most effective methods to improve the oxidation resistance of Ti_3SiC_2 is the substitution of a transition metal element for Ti. For example, our previous works[31,32] show that the Nb doped Ti_3SiC_2 solid solutions significantly improve the oxidation resistance of Ti_3SiC_2. What's more, these solutions possess better oxidation resistance and lower ASR than two typical metallic interconnects, Crofer 22APU and E-brite. $(Ti_{1-x}Nb_x)_3SiC_2$ is a great potential material in the application as an interconnect for IT-SOFC. After Nb doping, the oxidation rate of $(Ti,Nb)_3SiC_2$ decreases remarkably. The reduction concentration of oxygen vacancies and titanium interstitials in rutile TiO_2 (r-TiO_2) by Nb doping is the main reason. Interestingly, the post-oxidation ASR of $(Ti,Nb)_3SiC_2$ is also decreased greatly.[31]

As in the same transition element group with Nb, Ta ion also possesses penta-valence after ionization. The ionic radium for Ti^{4+}, Nb^{5+}, and Ta^{5+} is 0.068 nm, 0.069 nm, and 0.070 nm, respectively. The ionic radium difference of Ta with Ti is larger than that of Nb with Ti. It is reasonable to believe that Ta doped Ti_3SiC_2 may exhibit more suitable performance than Nb doped any other metallic interconnect. In this paper, the Ta doped Ti_3SiC_2 solution is successfully synthesized, and the oxidation behaviours and electrical property of this solid solution are investigated at 800 °C in air up to 500 h. We aim to not only explore a novel and promising interconnects for SOFC, but also study the effect mechanism of Ta on the oxidation behaviours and electrical property of Ti_3SiC_2.

2. Experimental

5 at% Ta doped Ti_3SiC_2 bulk material was fabricated by *in situ* solid–liquid reaction/hot pressing process. The raw powders of titanium, tantalum, silicon and graphite were selected at a molar ratio of 2.85 : 0.15 : 1 : 2. The final solid solution was denoted as $(Ti_{0.95}Ta_{0.05})_3SiC_2$ according to the nominal apportions of the raw powders. To avoid the appearance of a second phase of TiC, a little Al powder was also added to the raw powders. All raw powders were mixed and milled in a polypropylene jar for 24 h. After ball milling, the powders were cool pressed uniaxially under 5 MPa in a graphite die with a diameter of 50 mm. The *in situ* reaction/hot press sintering was carried out at 1580 °C under a pressure of 30 MPa for 1 h in flowing Ar atmosphere. The predominant phase for the as-synthesized solid solution was Ti_3SiC_2, and small quantities of $(Ti,Ta)Si_2$ and $(Ti,Ta)_5Si_2$ impurities also appeared. Compared to that of pure Ti_3SiC_2, the peak corresponding to the (101) lattice plane of $(Ti_{0.95}Ta_{0.05})_3SiC_2$ shifted to a lower angle (about 0.036°). It revealed that the rutile lattice parameter corresponding to (101) plane had increased. The EDS surface scanning on the $(Ti_{0.95}Ta_{0.05})_3SiC_2$ crystal grain (not shown here for abbreviation) showed that Ta was in the grain, and the atomic ratio of Ta/(Ti + Ta) was about 5%. From the above results, it was deduced that Ta had been doped into Ti_3SiC_2 lattice, and the lattice parameter of Ti_3SiC_2 had been changed because Ta had a larger radius than Ti. The density of the solid solution was determined by the Archimedes method in which three parallel samples were tested to acquire the mean value. The density of this solid solution was 4.92 ± 0.02 g cm^{-3}, and the relative density was ~99.2%.

For oxidation tests, 10 × 10 × 2 mm square coupons were cut from the as-synthesized bulk by the electrical discharge method. Prior to oxidation, the surfaces of the samples were grounded down to 2000 SiC paper, chamfered, polished using 1 μm diamond paste, and then degreased in ethanol and distilled water.

Oxidation tests were carried out in a tube furnace at 800 °C in air for up to 500 h. In the whole oxidation period, the step sequence was as follows: (1) the samples were heated up to 800 °C with furnace heating; (2) after every 100 h of isothermal oxidation at 800 °C, the samples were cooled down rapidly to room temperature in air; (3) the samples were weighed using a microbalance with an accuracy of 1×10^{-5} g; (4) the samples were then put into the hot furnace again.

The oxidation products were identified by X-ray diffraction (XRD) in a D/max -2500PC diffractometer (Rigaku, Tokyo, Japan) with Cu Kα radiation. The morphologies of the surface and the cross-section of the oxide scale formed on the matrix were observed by the SUPRA35 scanning electron microscope (SEM, LEO, Oberkochen, Germany). This SEM is equipped with an energy-dispersive spectroscopy (EDS, INCA, Oxford Instrument, Oxford, U.K.) system. Before SEM examination, a thin layer of Au was evaporated on the surface of the oxidized sample.

The electrical conductivity of $(Ti_{0.95}Ta_{0.05})_3SiC_2$ after oxidation was determined by the 2-probe 4-point method in static air. The ASR was adopted to evaluate the electrical property of the oxidized coupons. ASR can reflect the integrated effect of both electrical resistivity and thickness of the oxide scale. To ensure the tight surface contact, Pt mesh was used, and Pt-paste was applied as a high temperature conductive adhesive. A constant current with 10 mA was supplied by the Precision Programmable Current Source (YL4012), and the corresponding voltage drop was recorded continuously by the FLUKE 8845A 6-1/2 Digit Programmable Multimeter.

3. Results and discussion

3.1 Oxidation behaviour

3.1.1 Oxidation kinetics. Fig. 1(a) shows the mass gains per unit area *vs.* time of $(Ti_{0.95}Ta_{0.05})_3SiC_2$ after oxidation at 800 °C in air for 500 h. For comparison, the oxidation kinetics of $(Ti_{0.95}Nb_{0.05})_3SiC_2$ and Crofer 22 APU[33] oxidized under the same condition are also shown. It can be seen that the mass gain of $(Ti_{0.95}Ta_{0.05})_3SiC_2$ increases continuously during the whole oxidation process, suggesting that no spallation happens. This is in accordance with results that show no weight increase for the quartz boat where the samples are hung during oxidation procedure. Compared with $(Ti_{0.95}Nb_{0.05})_3SiC_2$ and Crofer 22 APU, the weight gain of $(Ti_{0.95}Ta_{0.05})_3SiC_2$ is lower. The Ta doped Ti_3SiC_2 possesses better oxidation resistance than Nb doped Ti_3SiC_2 and the metallic interconnect of Crofer 22 APU. As Ta radius is larger than the Nb radius, substituting Ti in the place of Ta in the rutile lattice may result in larger lattice distortions. Then the transportation of ions through the Ta

Open Access Article. Published on 01 September 2017. Downloaded on 11/23/2025 1:03:58 PM.
This article is licensed under a Creative Commons Attribution 3.0 Unported Licence.

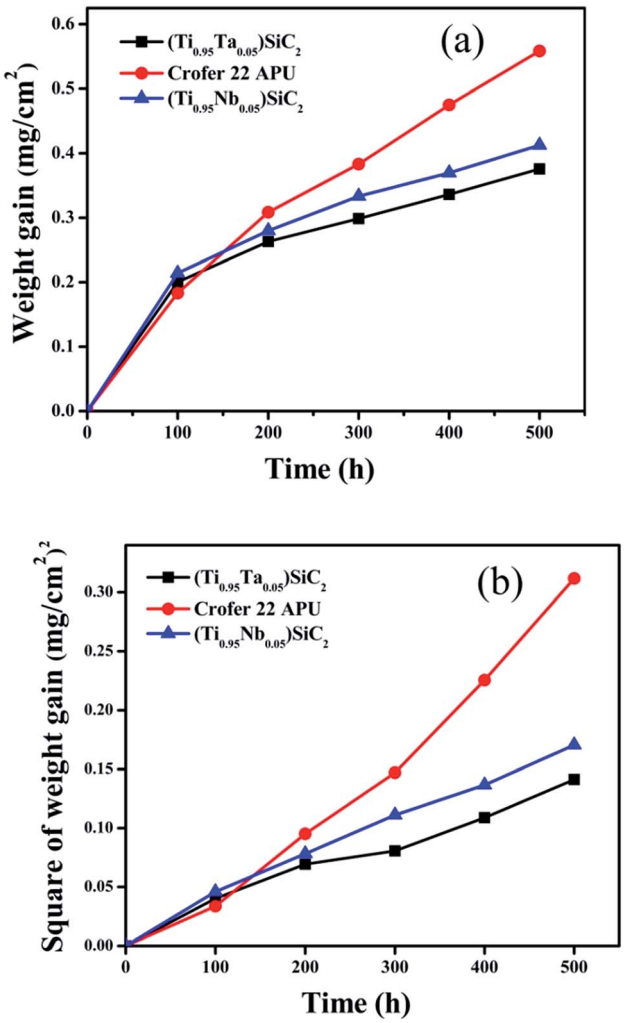

Fig. 1 Weight gain per unit area *vs.* time (a) and square of weight gain per unit area *vs.* time (b) of $(Ti_{0.95}Ta_{0.05})_3SiC_2$, $(Ti_{0.95}Nb_{0.05})_3SiC_2$ and Crofer 22 APU at 800 °C in air.

doped rutile crystal will be slower than that through the Nb doped one. Therefore, the oxidation resistance of Ta doped Ti_3SiC_2 is better than the Nb doped one; this will be further studied in the future. Fig. 1(b) presents the square of mass gain per unit *vs.* oxidation time of $(Ti_{0.95}Ta_{0.05})_3SiC_2$ for the oxidation at 800 °C. The nearly linear regular pattern reveals that the oxidation kinetics of $(Ti_{0.95}Ta_{0.05})_3SiC_2$ obeys a parabolic law as the formula (1) shows:

$$(\Delta w/A)^2 = k_p t \quad (1)$$

where, k_p is the oxidation rate constant, Δw is the mass gain of the sample, A is the area of the oxidized sample, and t is the oxidation time. As the oxidation kinetics of $(Ti_{0.95}Ta_{0.05})_3SiC_2$ follows a parabolic law, it can be inferred that the oxidation process of $(Ti_{0.95}Ta_{0.05})_3SiC_2$ is controlled by the diffusion of ions through the formed oxide scale, which is the same as $(Ti_{0.95}Nb_{0.05})_3SiC_2$ and Crofer 22 APU. By fitting the oxidation kinetics, the oxidation rate constant of $(Ti_{0.95}Ta_{0.05})_3SiC_2$ was determined as 7.33×10^{-14} g^2 cm^{-4} s^{-1}. For comparison the oxidation rate constants of $(Ti_{0.95}Ta_{0.05})_3SiC_2$, $(Ti_{0.95}Nb_{0.05})_3SiC_2$, Ti_3SiC_2 and Crofer 22 APU are also summarized in Table 1.

From Table 1, it can be seen that after Ta doping, the oxidation resistance of Ti_3SiC_2 is improved. And its oxidation rate constant is decreased by approximate one order of magnitude than that of Ti_3SiC_2. Compared with Nb doping, Ta doping exhibits a better effect on improving the oxidation resistance of Ti_3SiC_2.

3.1.2 Phase composition and morphology of the oxide production. Fig. 2 shows the XRD patterns of the oxide production formed on the $(Ti_{0.95}Ta_{0.05})_3SiC_2$ after oxidation. It can be seen that the main oxide scale is r-TiO_2 with little of Al_2O_3. It needs to be noted that the XRD peaks originated from the substrate, while Ti_3SiC_2 is the main phase with some (Ti,Ta)Si_2 and $(Ti,Ta)_5Si_2$ impurities. This shows that the formed oxide scale is very thin and leads to the appearance of matrix phases. At the same time, the Pt is detected by XRD. This Pt comes from the Pt paste which is brushed on the sample surface as conductive adhesive. As there is no Ta oxide formed in the oxide scale, it is deduced that Ta has doped into the TiO_2 lattice. Fig. 2(b) exhibits the fine structure of the (110) peak of r-TiO_2 formed on $(Ti_{0.95}Ta_{0.05})_3SiC_2$ and Ti_3SiC_2 oxidized under the same conditions. It can be clearly seen that compared with r-TiO_2 on Ti_3SiC_2, the (110) peak of r-TiO_2 formed on $(Ti_{0.95}Ta_{0.05})_3SiC_2$ shifts to lower angles, which indicates that Ta has doped into the r-TiO_2 lattice and induces rutile crystal lattice distortions.

Fig. 3 exhibits the surface morphologies of $(Ti_{0.95}Ta_{0.05})_3SiC_2$ after oxidation. The contour of the substrate is clearly visible, which indicates that the oxide scale is very thin. This is in accordance with the XRD results. Meanwhile, some abnormal areas exist on the surface marked in the rectangular portion in Fig. 3. It is the oxide scale formed on (Ti,Ta)Si_2 and $(Ti,Ta)_5Si_2$ identified by EDS (the EDS results are not shown here for abbreviate). These impurities possess different oxidation rates from that of the matrix phase, leading to the rough surface on the oxidized sample.

Fig. 4 illustrates the cross-section morphology of the oxide scales formed on $(Ti_{0.95}Ta_{0.05})_3SiC_2$ and corresponding with EDS elements line-scanning profiles along the red line. It clearly shows that the oxide scale formed on $(Ti_{0.95}Ta_{0.05})_3SiC_2$ is a monolithic layer, and the thickness is approximate 3 μm. No void or local spallation is found at the oxide/substrate interface, implying good adherence between the oxide monolithic layer and the substrate. The samples have experienced five thermal

Table 1 The oxidation rate constants of $(Ti_{0.95}Ta_{0.05})_3SiC_2$, Ti_3SiC_2, $(Ti_{0.95}Nb_{0.05})_3SiC_2$ and Crofer 22 APU at 800 °C in air

Material	Mass gain after 500 h oxidation (g cm^{-2})	k_p (g^2 cm^{-4} s^{-1})
Ti_3SiC_2	1.01	5.64×10^{-13}
$(Ti_{0.95}Ta_{0.05})_3SiC_2$	0.38	7.33×10^{-14}
$(Ti_{0.95}Nb_{0.05})_3SiC_2$	0.41	9.18×10^{-14}
Crofer 22 APU	0.56	1.71×10^{-13}

 This journal is © The Royal Society of Chemistry 2017

Open Access Article. Published on 01 September 2017. Downloaded on 11/23/2025 1:03:58 PM.
This article is licensed under a Creative Commons Attribution 3.0 Unported Licence.

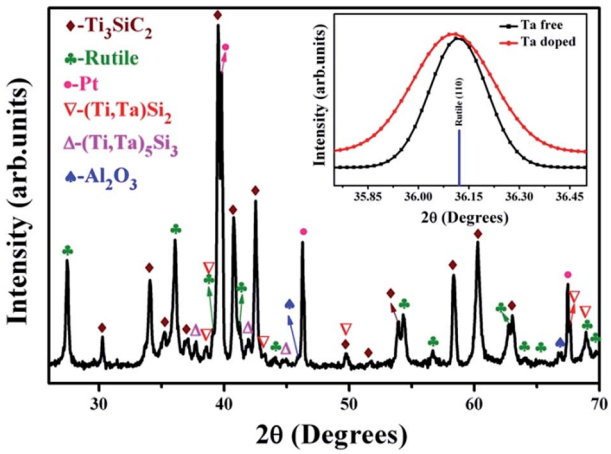

Fig. 2 XRD pattern of $(Ti_{0.95}Ta_{0.05})_3SiC_2$ after oxidation at 800 °C in air for 500 hours; the inserted figure is comparison of (101) peak position of r-TiO_2 formed on $(Ti_{0.95}Ta_{0.05})_3SiC_2$ and Ti_3SiC_2 after oxidation at 800 °C in air for 500 hours.

cycles from room temperature to 800 °C in air. The fine interface can avoid electron scattering and allows for electron transportation through the interface. From the EDS line scanning, it can be known that the monolithic oxide layer is rich in Ti, Si, O and shows traces of Ta. Because the content is negligible, Al is not detected. Ti and Ta elements are distributed uniformly in the oxide layer. For Si, however, a higher content is found near the substrate than near the outer surface of the oxide layer. While a notable amount of Si element is detected in the oxide layer, no Si-containing oxide is identified by XRD. Therefore, it can be deduced that SiO_2 exists in an amorphous form in the oxide layer. The formation of amorphous SiO_2 has also been found during the oxidation of Ti_3SiC_2,[34–37] Ti_5Si_3,[38] $MoSi_2$,[39] and Si_3N_4.[40] Therefore, it can be concluded that the single oxide layer consists of a mixture of Ta doped r-TiO_2, amorphous SiO_2 and a little of Al_2O_3. The previous works[31] present that the oxide scale formed on Ti_3SiC_2 is composed of a double-layer and the

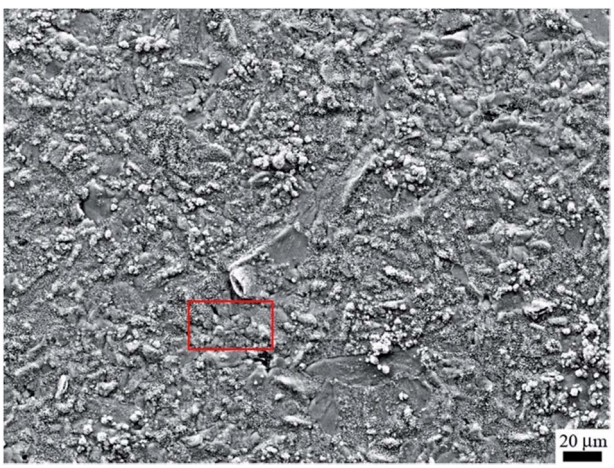

Fig. 3 Surface morphology of $(Ti_{0.95}Ta_{0.05})_3SiC_2$ after oxidation at 800 °C in air for 500 hours.

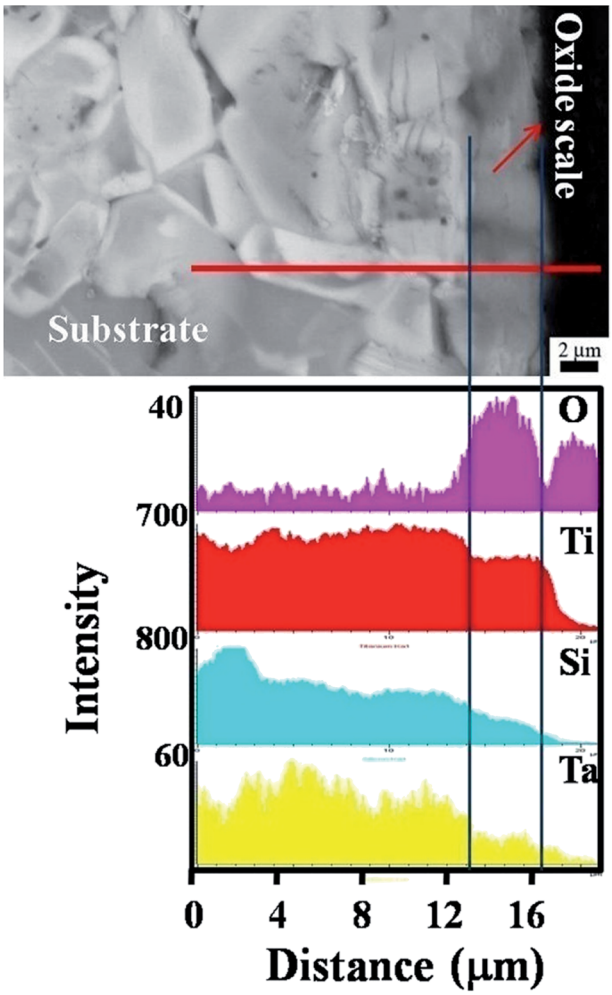

Fig. 4 Cross-section morphology and EDS line scanning taken across the oxide scale formed on $(Ti_{0.95}Ta_{0.05})_3SiC_2$ after oxidation at 800 °C in air for 500 hours.

thickness of the oxide layers is about 7 μm. The above results reveal that like Nb, Ta addition can also enhance the oxidation resistance of Ti_3SiC_2 and change the oxide layer structure from a duplex-layer to a monolithic layer structure. In addition, it is found that the morphology of plate-like grain in the matrix is clearly visible, which reveals that the $(Ti_{0.95}Ta_{0.05})_3SiC_2$ structure is stable without phase and grain morphology change.

3.2 Electrical conductivity

The electrical conductivity of the interconnect under the SOFC atmosphere is significant, because the interconnect electrically connects adjacent cells. Like metallic interconnects, $(Ti_{0.95}Nb_{0.05})_3SiC_2$ and Ti_3SiC_2, the substrates of $(Ti_{0.95}Ta_{0.05})_3SiC_2$ ceramics, have much higher electrical conductivity than its corresponding oxide scales even at 800 °C.[41] Therefore, the electrical resistance of $(Ti_{0.95}Ta_{0.05})_3SiC_2$ after oxidation is mainly contributed from the oxide scale formed on the surface. Fig. 5 presents the ASR of $(Ti_{0.95}Ta_{0.05})_3SiC_2$ after oxidation at 800 °C in air for 500 h. For comparison, the results for $(Ti_{0.95}Nb_{0.05})_3SiC_2$, Ebrite and Crofer 22 APU[33] are also presented. It can be seen that the

Open Access Article. Published on 01 September 2017. Downloaded on 11/23/2025 1:03:58 PM.
This article is licensed under a Creative Commons Attribution 3.0 Unported Licence.

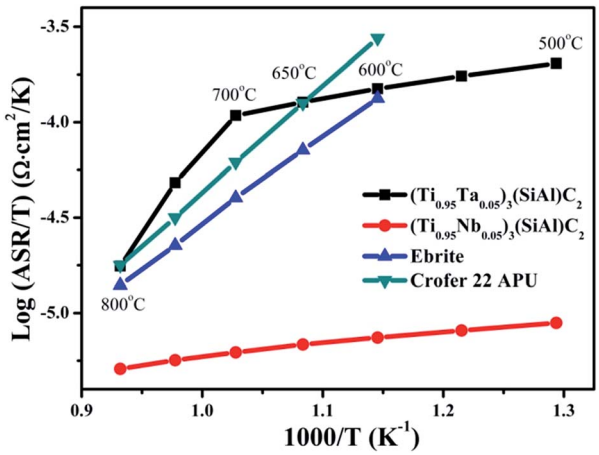

Fig. 5 Temperature dependencies of ASR of $(Ti_{0.95}Ta_{0.05})_3SiC_2$, $(Ti_{0.95}Nb_{0.05})_3SiC_2$, Ebrite, and Crofer 22 APU after oxidation at 800 °C in air.

curve for $(Ti_{0.95}Ta_{0.05})_3SiC_2$ is in agreement with a line law, and the slope of the curve changes at 700 °C. When the temperature is higher than 600 °C and 650 °C, the ASR of $(Ti_{0.95}Ta_{0.05})_3SiC_2$ is larger than that of Ebrite and Crofer 22 APU, respectively. The main oxide formed on Crofer 22 APU is Cr_2O_3. As the electrical resistance *vs.* temperature of Cr_2O_3 nearly obeys the line law, it is deduced that the ASR of $(Ti_{0.95}Ta_{0.05})_3SiC_2$ after oxidation is smaller than that of Ebrite and Crofer 22 APU below 600 °C and 650 °C, respectively. It is suggested that the electrical conductivity of $(Ti_{0.95}Ta_{0.05})_3SiC_2$ as an interconnect is better than Ebrite and Crofer 22 APU when SOFC service temperature is lower than 600 °C and 650 °C, respectively. The ASR of $(Ti_{0.95}Ta_{0.05})_3SiC_2$ is larger than that of $(Ti_{0.95}Nb_{0.05})_3SiC_2$ in the temperature range of 500–800 °C. The Ta doping effect on reducing ASR for the oxide scale is not as good as that of Nb. It may be caused by the higher electrical resistance of Ta doped TiO_2 than that of the Nb doped one.[42] The ASR of $(Ti_{0.95}Ta_{0.05})_3SiC_2$ at 800 °C after oxidation at the same temperature in air for 500 h is 29.5 mΩ cm^2, which is lower than that of Ti_3SiC_2 (85.0 mΩ cm^2) treated under the same conditions for 20 h. This suggests that Ta addition greatly improved the electrical conductivity of post-oxidized Ti_3SiC_2.

3.3 Mechanism of Ta doping effect

From the previous results, it is known that after Ta doping, the oxidation resistance of Ti_3SiC_2 is enhanced and becomes even better than that of Nb. Furthermore, after Ta doping, the oxide scale layer of Ti_3SiC_2 is changed from a duplex-layer to a monolithic layer of Ta doped r-TiO_2, amorphous SiO_2 and a small amount of Al_2O_3.

The oxygen diffusion coefficient of TiO_2 and the electronic conductivity of TiO_2 are much higher than those of SiO_2. The oxidation of $(Ti_{0.95}Ta_{0.05})_3SiC_2$ is controlled by the diffusion of ions though the oxide scale. The ion diffusion through the oxide scale, especially through the lattice of TiO_2, is the control step. For the electrical conductivity of the oxidized $(Ti_{0.95}Ta_{0.05})_3SiC_2$, the ASR depends on the formed oxide scale (r-TiO_2 and amorphous SiO_2), which especially depends on the electron diffusion through the r-TiO_2. Therefore, it is deduced that Ta addition increases the oxidation resistance and the electrical conductivity of Ti_3SiC_2 after oxidation, mainly by affecting the transmission of ions and electrons through r-TiO_2.

TiO_2 is an n-type semiconductor and oxygen vacancies, tri- and quadri-valent Ti interstitials exist as native defects. When penta-valent Ta ions are doped into r-TiO_2 lattice, the donation energy level of Ta produces an energy band. According to the defect chemistry theory, the following defect chemistry reaction will be proposed in an air atmosphere[43–45] (expressed as Kröger and Vink's defect symbols[46,47]):

$$2Ta_2O_5 \xleftrightarrow{TiO_2} 4Ta_{Ti}^{\cdot} + 10O_O^{\times} + V_{Ti}^{''''} \quad (2)$$

This means that after Ta is doped into the r-TiO_2 lattice, the vacancy of Ti is produced. As there are oxygen vacancies, tri- and quadri-valent Ti interstitials in the r-TiO_2 lattice, after the vacancy of Ti is generated, the following equilibrium will take place:

$$V_{Ti}^{''''} + Ti_{Ti}^{4+} \leftrightarrow Ti_{Ti} \quad (3)$$

$$V_{Ti}^{''''} + 2V_O^{\cdot\cdot} \leftrightarrow nil \quad (4)$$

Furthermore, the following reaction will happen after reaction (4):

$$O_O^{\times} \leftrightarrow V_O^{\cdot\cdot} + 2e' + 1/2O_2 \quad (5)$$

The equilibrium constant of reaction (5) can be expressed as:

$$K = [V_O^{\cdot\cdot}]n^2 P_{O_2}{}^{1/2} \quad (6)$$

where, K is the balance constant, n denotes the concentration of semi-free electrons, the brackets [] denote the concentration of defects in site, and P_{O_2} is the pressure of oxygen.

The above equilibriums (3) and (4) mean that after vacancy of Ti is produced, the Ti interstitial and oxygen vacancy will react with the vacancy of Ti. This will lead to a decrease in the concentration of Ti interstitial as well as oxygen vacancy in r-TiO_2. Therefore, it is deduced that Ta doping decreases the outward diffusion of Ti by decreasing the concentration of native Ti interstitials and simultaneously restraining the inward diffusion of oxygen by decreasing the concentration of O vacancies. As a result, after Ta doping in Ti_3SiC_2, the oxidation resistance of Ti_3SiC_2 enhances remarkably, the oxidation rate constant decreases about one order of magnitude, and the oxide structure changes from a duplex-layer to a single mixture layer.

At the same time, when reaction (4) happens, the $V_O^{\cdot\cdot}$ decreases. Then, according to equilibrium (6), the electron concentration of "n" in r-TiO_2 correspondingly increases. This means that the electrical conductivity of the Ta doped TiO_2 will increase. This can be the main reason for the lower ASR of $(Ti_{0.95}Ta_{0.05})_3SiC_2$ after oxidation compared to that of the undoped Ti_3SiC_2.

Open Access Article. Published on 01 September 2017. Downloaded on 11/23/2025 1:03:58 PM. This article is licensed under a Creative Commons Attribution 3.0 Unported Licence.

4. Conclusions

The oxidation behaviours and electrical property of 5 at% Ta doped Ti_3SiC_2 solid solution has been investigated at 800 °C in air up to 500 h. The following conclusions are drawn:

(1) The oxidation kinetics of $(Ti_{0.95}Ta_{0.05})_3SiC_2$ follows parabolic law, and the oxidation rate constant is 7.33×10^{-14} g^2 cm^{-4} s^{-1}, which is lower than that of Ti_3SiC_2, $(Ti_{0.95}Nb_{0.05})_3SiC_2$ and Crofer 22 APU.

(2) The ASR of $(Ti_{0.95}Ta_{0.05})_3SiC_2$ at 800 °C after oxidation at 800 °C in air for 500 h is 29.5 mΩ cm^2, which is much lower than that of Ti_3SiC_2. Ta addition greatly improved the electrical conductivity of Ti_3SiC_2 after oxidation. The ASR of $(Ti_{0.95}Ta_{0.05})_3SiC_2$ will be smaller than that of Ebrite and Crofer 22 APU when the temperature is lower than 600 °C and 650 °C, respectively.

(3) Ta doping can decrease the outward diffusion of Ti by decreasing the concentration of native Ti interstitials. Meanwhile, this restrains the inward diffusion of oxygen by decreasing the concentration of O vacancies. This results in the enhanced oxidation resistance of Ti_3SiC_2 and the changed oxide layer structure from a double-layer to a single mixture layer.

(4) The increased concentration of electrons in r-TiO_2 by Ta doping results in increased electrical conductivity of the –TiO_2. This is the main reason for the lower ASR of $(Ti_{0.95}Ta_{0.05})_3SiC_2$ after oxidation compared to that of Ti_3SiC_2.

Conflicts of interest

There are no conflicts to declare.

Acknowledgements

This work was financially supported by the National Science Foundation of China (Grant No. 51271191, 51571205 and 41406106), and the Scientific Research Start-up Fund of Qingdao University (Grant No. 41117010089).

Notes and references

1 N. Q. Minh, *J. Am. Ceram. Soc.*, 1993, **76**, 563.
2 J. W. Fergus, *Mater. Sci. Eng., A*, 2005, **397**, 271.
3 Z. G. Yang, K. S. Weil, D. M. Paxton and J. W. Stevenson, *J. Electrochem. Soc.*, 2003, **150**(9), A1188.
4 W. Z. Zhu and S. C. Deevi, *Mater. Sci. Eng., A*, 2003, **348**, 227.
5 T. Ishihara, H. Matsuda and Y. Takita, *J. Am. Chem. Soc.*, 1994, **116**, 3801.
6 S. D. Souza, S. J. Visco and L. C. D. Jonghe, *J. Electrochem. Soc.*, 1997, **144**, L35.
7 P. Huang and A. Petric, *J. Electrochem. Soc.*, 1996, **143**, 1644.
8 M. Dokiya, *Solid State Ionics*, 2002, **152**, 383.
9 M. F. Han, S. Peng, Z. Wang, Z. Yang and X. Chen, *J. Power Sources*, 2007, **164**, 278.
10 S. P. S. Badwal, R. Deller, K. Foger, Y. Ramprakash and J. P. Zhang, *Solid State Ionics*, 1997, **99**, 297.
11 K. H. Joa, J. H. Kimb, K. M. Kimb, I. S. Leec and S. J. Kim, *Int. J. Hydrogen Energy*, 2015, **40**, 9523.
12 Z. G. Yang, M. S. Walker, P. Singh, J. W. Stevenson and T. Norby, *J. Electrochem. Soc.*, 2004, **151**(12), B669.
13 R. Sachitanand, M. Sattari, J. E. Svensson and J. Froitzheim, *Int. J. Hydrogen Energy*, 2013, **38**, 15328.
14 S. J. Geng, J. H. Zhu and Z. G. Lu, *Solid State Ionics*, 2006, **177**, 559.
15 P. Piccardo, S. Anelli, V. Bongiorno, R. Spotorno, L. Repetto and P. Girardon, *Int. J. Hydrogen Energy*, 2015, **40**, 3726.
16 J. Froitzheim, G. H. Meier, L. Niewolak, P. J. Ennis, H. Hattendorf, L. Singheiser and W. J. Quadakkers, *J. Power Sources*, 2008, **178**, 163.
17 B. Hua, J. Pu, F. S. Lu, J. F. Zhang, B. Chi and L. Jian, *J. Power Sources*, 2010, **195**, 2782.
18 S. Swaminathan, Y. S. Lee and D. I. Kim, *J. Power Sources*, 2016, **327**, 104.
19 P. D. Jablonski and D. E. Alman, *J. Power Sources*, 2008, **180**, 433.
20 S. J. Geng, J. H. Zhu, M. P. Brady, H. U. Anderson, X. D. Zhou and Z. G. Yang, *J. Power Sources*, 2007, **172**, 775.
21 B. K. Park, D. W. Kim, R. H. Song, S. B. Lee, T. H. Lim, S. J. Park, C. O. Park and J. W. Lee, *J. Power Sources*, 2015, **300**, 318.
22 W. J. Shong, C. K. Liu, S. H. Wua, H. C. Liu and P. Yang, *Int. J. Hydrogen Energy*, 2014, **39**, 19737.
23 X. N. Hosseini, M. H. Abbasi, F. Karimzadeh and G. M. Choi, *J. Power Sources*, 2015, **273**, 1073.
24 J. G. Grolig, P. Alnegren, J. Froitzheim and J. E. Svensson, *J. Power Sources*, 2015, **297**, 534.
25 Z. G. Yang, G. G. Xi and J. W. Stevenson, *Electrochem. Solid-State Lett.*, 2005, **8**(3), A168.
26 A. Harthoj, T. Holt and P. Møller, *J. Power Sources*, 2015, **281**, 227.
27 A. M. Ruiz, K. Vidal, A. Larrañaga, J. M. P. Vázquez, P. R. Slater and M. I. Arriortua, *Int. J. Hydrogen Energy*, 2015, **40**, 8407.
28 N. Shaigana, W. Qua, D. G. Iveyb and W. X. Chen, *J. Power Sources*, 2010, **195**, 1529.
29 M. W. Barsoum and T. El-Raghy, *J. Am. Ceram. Soc.*, 1996, **79**, 1953.
30 Y. C. Zhou and Z. M. Sun, *Mater. Res. Innovations*, 1999, **2**, 360.
31 L. L. Zheng, X. C. Li, Q. S. Hua, Z. Q. Dai, T. Z. Zhang, Y. H. Qian, J. J. Xu and M. S. Li, *J. Am. Ceram. Soc.*, 2017, **100**, 1.
32 L. L. Zheng, J. J. Li, M. S. Li and Y. C. Zhou, *Int. J. Hydrogen Energy*, 2012, **37**, 1084.
33 S. J. Geng, J. H. Zhu and Z. G. Lu, *Scr. Mater.*, 2006, **55**, 239.
34 Z. M. Sun, Y. C. Zhou and M. S. Li, *Corros. Sci.*, 2001, **43**, 1095.
35 Z. M. Sun, Y. C. Zhou and M. S. Li, *Acta Mater.*, 2001, **49**, 4347.
36 M. W. Barsoum, T. El-Raghy and L. U. J. T. Ogbuji, *J. Electrochem. Soc.*, 1997, **144**, 2508.
37 C. Racault, F. Langlais and R. Naslain, *J. Mater. Sci.*, 1994, **29**, 3384.
38 H. Jiang, C. S. Petersson and M. A. Nicolet, *Thin Solid Films*, 1986, **140**, 115.

39 C. G. Mckamey, P. F. Tortorelli, J. H. DeVan and C. A. Carmichael, *J. Mater. Res.*, 1992, **7**, 2747.
40 Y. G. Gogotsi and F. Porz, *Corros. Sci.*, 1992, **33**, 627.
41 M. W. Barsoum, *Prog. Solid State Chem.*, 2000, **28**, 201.
42 D. M. Chen, G. Xu, L. Miao, S. Nakao and P. Jin, *Surf. Coat. Technol.*, 2011, **206**, 1020.
43 T. Bak, J. Nowotny, M. Rekas and C. C. Sorrell, *J. Phys. Chem. Solids*, 2003, **64**, 1043.
44 T. Bak, J. Nowotny, M. Rekas and C. C. Sorrell, *J. Phys. Chem. Solids*, 2003, **64**, 1057.
45 T. Bak, J. Nowotny, M. Rekas and C. C. Sorrell, *J. Phys. Chem. Solids*, 2003, **64**, 1069.
46 F. A. Kröger and H. J. Vink, *Solid State Phys.*, 1956, **3**, 307.
47 M. F. Yan and W. W. Rhodes, Additives and interfaces in electronic ceramics, in *Advances in Ceramics*, ed. M. F. Yan and A. H. Heuer, American Ceramic Society, Columbus, OH, 1983, pp. 226–238.

Open Access Article. Published on 01 September 2017. Downloaded on 11/23/2025 1:03:58 PM.
This article is licensed under a Creative Commons Attribution 3.0 Unported Licence.

 This journal is © The Royal Society of Chemistry 2017